MJFAS
Malaysian Journal of Fundamental and Applied Sciences

Mohd Daud *et al.* | Malaysian Journal of Fundamental and Applied Sciences, Vol. 21 (2025) 2997–3018

RESEARCH ARTICLE

MHD Free Convection Boundary Layer Flow on a Horizontal Circular Cylinder in a Williamson Hybrid Ferrofluid under Heat Generation/Absorption

Marjan Mohd Daud[a], Norhafizah Md Sarif[a], Huei Ruey Ong[b] and Muhammad Khairul Anuar Mohamed[a,*],

[a]Centre for Mathematical Sciences, Universiti Malaysia Pahang Al-Sultan Abdullah, Lebuh Persiaran Tun Khalil Yaakob, 26300 Kuantan, Pahang, Malaysia; [b]Faculty of Engineering & Technology, DRB-HICOM University of Automotive Malaysia, Peramu Jaya Industrial Area, 26607, Pekan, Pahang, Malaysia

Abstract This study investigates the free convection boundary layer flow past a horizontal circular cylinder immersed in Williamson hybrid ferrofluid. Magnetite (Fe_3O_4) and gold (Au) nanoparticles are suspended in blood which serves as the non-Newtonian Williamson based fluid. The effects of heat generation/absorption and magnetohydrodynamic (MHD) were incorporated into the mathematical formulation. The governing nonlinear partial differential equations describing the flow and heat transfer phenomena are non-dimensionalized and reduced to a system of ordinary differential equations. These equations were solved numerically using the Keller-box implicit finite difference method. The Keller-box algorithm is implemented in MATLAB software to compute the graphical representations, and the influence of pertinent parameters on skin friction coefficient, Nusselt number, velocity and temperature profiles. The results show that the hybrid ferrofluid significantly exhibits superior convective heat transfer and skin friction performance compared to conventional ferrofluids containing only a single type of nanoparticle. Moreover, the presence of heat generation/absorption was found to strongly influence the thermal boundary layer thickness, providing new insights into the optimization of hybrid ferrofluids for engineering and biomedical applications.

Keywords: Williamson hybrid ferrofluid, Keller-box method, magnetite nanoparticles, gold nanoparticles

***For correspondence:**
mkhairulanuar@umpsa.edu.my

Received: 3 Jan. 2024
Accepted: 28 Oct. 2025

Introduction

Convective heat transfer plays a vital role in numerous industrial and biomedical applications, including heat exchangers, solar collectors, electronic cooling systems, and physiological transport processes [1]. There are three types of convection which are free convection, forced convection and mixed convection. Among these types, stated by Mauri [2], free convection is particularly significant due to its occurrence in situations where fluid motion is induced solely by buoyancy forces resulting from temperature gradient. Consequently, gaining insight into free convection boundary layer phenomena is fundamental to improving the design efficiency of thermal systems. In recent years, numerous studies have focused on conventional heat transfer fluids such as water, oils, and ethylene glycol. Despite their widespread use, these fluids suffer from inherently low thermal conductivity, which restricts their overall heat transfer performance [3-6].

Therefore, to overcome this limitation, researchers have explored on nanosized soled particles, immersed into base fluids, resulting in nanofluids. According to Borode *et al*. [7], the dispersion of metallic or non-metallic nanoparticles such as copper (*Cu),* aluminum oxide (Al_2O_3), titanium dioxide (TiO_2) and magnetite (Fe_3O_4) significantly enhances the fluid's thermophysical properties, viscosity, and convective heat transfer coefficient compared to pure base fluid creating a more effective medium for heat transport.

This innovation has led to remarkable progress in the field of nanotechnology. Consequently, nanofluids have been widely studied for their potential in energy conversion, microchannel cooling and medical applications [8-9].

Among the various classes of nanofluid, ferrofluids have attracted particular attention due to their unique magnetic properties. Introduced by Papell [10], this ferrofluid was originally developed to use in NASA's space technology applications. Specifically for stabilizing spinning shaft seals and enabling the controlled movement of rocket fuel under weightless conditions by magnetic fields. Since its invention, the development of ferrofluids has advanced considerably, with improved magnetic liquids and diverse base fluids. Oehlsen *et al*. [11] highlighted, ferrofluids are colloidal suspensions of ferromagnetic nanoparticles within a carrier fluid. The application of a magnetic field induces Lorentz forces that modify fluid motion and temperature distribution, enabling precise control of the flow behavior and heat transfer rate [12]. Since its invention, the development of ferrofluids has advanced considerably, with improved magnetic liquids and diverse base fluids. Their unique magnetics and thermal properties have attracted wide industrial and engineering interest. For instance, ferrofluids are utilized in loudspeakers to dissipate heat and suppress vibrations, employed in mineral processing to separate ores based on density variation under magnetic fields, and integrated into microfluidics as well as micromechanical devices [13-15].

Recently, the development of hybrid ferrofluids has opened new pathways for improving heat transfer performance due to their unique behavior. A hybrid ferrofluid contains two or more types of nanoparticles, designed to combine the favorable attributes of each component. For instance, magnetite (Fe_3O_4) nanoparticles provide strong magnetic response and stability, while gold (Au) nanoparticles exhibit excellent thermal conductivity and biocompatibility. Gold nanoparticles, once introduced into the bloodstream, can circulate freely through blood vessels owing to their nanoscale size and biocompatibility. In addition, by exploiting their ability to absorb energy and generate heat, they can induce hyperthermia that destroys cancerous cells while leaving surrounding tissues unharmed [16]. Importantly, gold is biocompatible and non-toxic in the human body, making it a favorable nanoparticle for therapeutic use. Consequently, gold nanoparticles highlight the synergy between nanotechnology and biomedicine, while also underscoring the need for further optimization in therapeutic delivery. Stated by Abdullah and Ismail [17], these hybrid ferrofluid make it particularly suitable for biomedical applications like targeted drug delivery, magnetic hyperthermia and biothermal regulation. Several researchers have reported superior convective heat transfer rates and improved thermal uniformity in hybrid ferrofluids compared to conventional ferrofluids [18-20].

In biomedical and physiological context, blood serves as a naturally occurring non-Newtonian fluid, often modelled using the Williamson model to capture its shear-thinning behavior. Its composition includes the presence of hemoglobin molecules containing ferrous ions, which are magnetically responsive. Due to these properties, the Navier–Stokes equations are insufficient to capture its rheological behavior, requiring modified mathematical models. The Williamson model, first introduced by Williamson [21] provides one framework to describe pseudoplastic flow. The integration of magnetic nanoparticles into blood can enhance its transport properties and enable external control via magnetic fields, which has potential applications in targeted drug delivery, hyperthermia treatment, and magnetic flow diagnostics [22-24]. Therefore, examining the heat and flow behavior of Williamson hybrid ferrofluids such as Fe_3O_4–Au/blood is of both scientific and practical importance.

In many practical thermal systems, such as high-performance electronic cooling, nuclear reactors and biomedical devices, internal heat generation or absorption within the fluid plays critical role [9,25]. This internal mechanism can drastically alter the thermal field, temperature gradients, and overall heat transfer performance. Despite its importance, the influence of internal heat generation or absorption is still relatively underexplored, particularly in studies involving hybrid ferrofluids flowing over curved geometries like horizontal cylinders. Such scenarios are more representative of real-world applications, where thermal sources or sinks within the medium often coexist with external heating or cooling processes. To better simulate realistic operating conditions, it is essential to include the effects of internal heat generation and absorption in the analysis of hybrid ferrofluid systems. This highlights a clear research gap, where coupling internal heat generation/absorption with hybrid ferrofluids over curved surfaces remains insufficiently studied.

The present study has important applications in both biomedical and engineering fields. Hybrid ferrofluids composed of Fe_3O_4–Au nanoparticles dispersed in blood are useful in medical technologies such as magnetic drug delivery and hyperthermia treatment due to their magnetic properties, good heat transfer performance and high biocompatibility. In engineering, magnetically controlled hybrid ferrofluids can enhance convective heat transfer in pipes, cooling channels and electromagnetic flow systems. The present model is unique as it integrates a Williamson non-Newtonian blood fluid with hybrid

nanoparticles, considering MHD and heat generation/absorption effects over a horizontal circular cylinder. This model has received limited attention in previous research and is introduced here to better represent the real behavior of blood flow under simultaneous magnetic and thermal influences. The result of this study is to provide new useful insight into improving the heat transfer performance and stability of hybrid ferrofluids for practical real-world applications.

Problem Formulation

In this study, a horizontal circular cylinder of radius a is examined while immersed in a hybrid ferrofluid environment. The surface of the cylinder is maintained at a constant temperature $\left(T_w\right)$ whereas the surrounding fluid far from the surface has a uniform temperature $\left(T_\infty\right)$, as depicted schematically in Figure 1. The coordinate system is set such that so that $\bar{x}$ - axis extends tangentially along the surface of the cylinder from the lower stagnation point $\left(\bar{x}=0\right)$, while $\bar{y}$ - axis is directed normally outward from the surface.

A constant magnetic field of uniform strength $\left(B_o\right)$ is imposed perpendicularly on the surface of the cylinder. Given that the magnetic Reynolds number is sufficiently small, the induced magnetic effects within the flow are considered negligible Under these physical conditions, the motion of the fluid and the associated heat transfer are governed by the steady-state free convection boundary-layer equations. These equations, formulated in their dimensional form, are derived under the assumption that the boundary-layer approximation remains valid for the present configuration [26,27,34].

$$\frac{\partial \bar{u}}{\partial \bar{x}}+\frac{\partial \bar{v}}{\partial \bar{y}}=0, \tag{1}$$

$$\begin{aligned}\bar{u}\frac{\partial \bar{u}}{\partial \bar{x}}+\bar{v}\frac{\partial \bar{u}}{\partial \bar{y}} &= \nu_{hnf}\frac{\partial^2 \bar{u}}{\partial \bar{y}^2}+\sqrt{2}\ \nu_{hnf}\Gamma\frac{\partial \bar{u}}{\partial \bar{y}}\frac{\partial^2 \bar{u}}{\partial \bar{y}^2} \\ &\quad +\frac{\left(\rho\beta\right)_{hnf}}{\rho_{hnf}}g(T-T_\infty)\sin\frac{\bar{x}}{a}-\frac{\sigma_{hnf}B_o^2}{\rho_{hnf}}\bar{u},\end{aligned} \tag{2}$$

$$\bar{u}\frac{\partial T}{\partial \bar{x}}+\bar{v}\frac{\partial T}{\partial \bar{y}}==\frac{k_{hnf}}{\left(\rho C_p\right)_{hnf}}\frac{\partial^2 T}{\partial \bar{y}^2}+\frac{Q_o}{\left(\rho C_p\right)_{hnf}}\left(T-T_\infty\right), \tag{3}$$

subjected to the suitable boundary conditions.

$$\begin{aligned}&\bar{u}(\bar{x},0)=\bar{v}(\bar{x},0)=0,\ T(\bar{x},0)=T_w,\\ &\bar{u}(\bar{x},\infty)\to 0,\ T(\bar{x},\infty)\to T_\infty,\end{aligned} \tag{4}$$

here, $\bar{u}$ is the velocity components of $\bar{x}$ axis, while $\bar{v}$ is the velocity components along the $\bar{y}$ axis. ν_{hnf} represent the hybrid ferrofluid's kinematic viscosity. ρ_{hnf}, β_{hnf} and μ_{hnf} denoted the density of hybrid nanofluid, thermal expansion of hybrid ferrofluid and dynamic viscosity of the hybrid ferrofluid, respectively. Meanwhile, g is gravitational acceleration and T is the local temperature. Next, k_{hnf} and $\left(\rho C_p\right)_{hnf}$ is the thermal conductivity of hybrid ferrofluid, and heat capacity of hybrid ferrofluid, respectively. Moreover, β_o and σ_{hnf} is the uniform magnetic field strength and electrical conductivity, correspondingly. To investigate the influence of internal heat generation or absorption, Q_o as the dimensional heat generation/absorption is introduced into the energy equation. When $Q_o>0$ implies the heat is generated inside the fluid, increasing the local temperature. Meanwhile, $Q_o<0$ indicates heat is absorbed, lowering the fluid temperature.

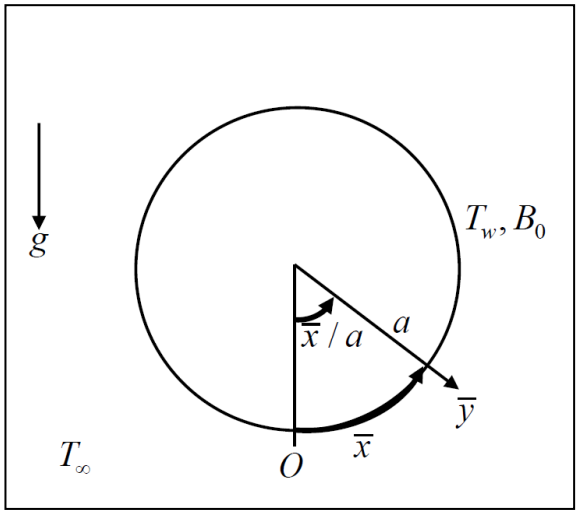

Figure 1. Physical model and the coordinate system

To demonstrate the qualities of the base fluid, hybrid ferrofluid and gold and ferromagnetic nanoparticles, the subscript $_{bf}$,$_{hnf}$ and $_{s1,s2}$ are used, respectively. Moreover, the solid volume fraction ϕ as follows [27,28]

$$\nu_{hnf}=\frac{\mu_{hnf}}{\rho_{hnf}},\ \mu_{hnf}=\frac{\mu_f}{(1-\phi_1)^{2.5}(1-\phi_2)^{2.5}},\ \rho_{hnf}=(1-\phi_2)\left[(1-\phi_1)\rho_f+\phi_1\rho_{s1}\right]+\phi_2\rho_{s2},$$

$$(\rho\beta)_{hnf}=(1-\phi_2)\left[(1-\phi_1)(\rho\beta)_f+\phi_1(\rho\beta)_{s1}\right]+\phi_2(\rho\beta)_{s2},$$

$$(\rho C_p)_{hnf}=(1-\phi_2)\left[(1-\phi_1)(\rho C_p)_f+\phi_1(\rho C_p)_{s1}\right]+\phi_2(\rho C_p)_{s2},$$

$$\frac{k_{hnf}}{k_{bf}}=\frac{k_{s2}+2k_{bf}-2\phi_2(k_{bf}-k_{s2})}{k_{s2}+2k_{bf}+\phi_2(k_{bf}-k_{s2})},\quad \frac{k_{bf}}{k_f}=\frac{k_{s1}+2k_f-2\phi_1(k_f-k_{s1})}{k_{s1}+2k_f+\phi_1(k_f-k_{s1})},$$

$$\frac{\sigma_{hnf}}{\sigma_{bf}}=\frac{\sigma_{s2}+2\sigma_{bf}-2\phi_2(\sigma_{bf}-\sigma_{s2})}{\sigma_{s2}+2\sigma_{bf}+\phi_2(\sigma_{bf}-\sigma_{s2})},\quad \frac{\sigma_{bf}}{\sigma_f}=\frac{\sigma_{s1}+2\sigma_f-2\phi_1(\sigma_f-\sigma_{s1})}{\sigma_{s1}+2\sigma_f+\phi_1(\sigma_f-\sigma_{s1})}.$$

The non-dimensional variables are introduced to transform the governing equations into non-dimensional equations.

$$x=\frac{\bar{x}}{a},\quad y=Gr^{1/4}\frac{\bar{y}}{a},\quad u=\frac{a}{\nu_f}Gr^{-1/2}\bar{u},\quad v=\frac{a}{\nu_f}Gr^{-1/4}\bar{v},\quad \theta(\eta)=\frac{T-T_\infty}{T_w-T_\infty}. \tag{5}$$

where θ and $Gr=\dfrac{g\beta_f(T_w-T_\infty)a^3}{\nu_f{}^2}$ are the dimensionless fluid's temperature and Grashof number, respectively. Applying equation (5), reduces the governing equations (1) – (3) and the boundary conditions (4), to non-dimensional equations as follows

$$\frac{\partial u}{\partial x}+\frac{\partial v}{\partial y}=0, \tag{6}$$

$$u\frac{\partial u}{\partial x}+v\frac{\partial u}{\partial y}=\frac{\nu_{hnf}}{\nu_f}\frac{\partial^2 u}{\partial y^2}+\frac{\sqrt{2}\Gamma\nu_f Gr^{3/4}}{a^2}\frac{\partial u}{\partial y}\frac{\partial^2 u}{\partial y^2} + \frac{(\rho\beta)_{hnf}}{\rho_{hnf}\beta_f}\theta\sin x-\frac{\sigma_{hnf}a^2}{\rho_{hnf}\nu_f Gr^{1/2}}B_o^2 u, \tag{7}$$

$$u\frac{\partial \theta}{\partial x}+v\frac{\partial \theta}{\partial y}=\frac{k_{hnf}}{\nu_f(\rho C_p)_{hnf}}\frac{\partial^2\theta}{\partial y^2}+\frac{a^2 Q_o}{\nu_f Gr^{1/2}(\rho C_p)_{hnf}}\theta, \tag{8}$$

The equations are subjected to

$$u(x,0)=0,\ v(x,0)=0,\ \theta(x,0)=1,\quad u(x,\infty)\to 0,\ \ \theta(x,\infty)\to 0 \tag{9}$$

Due to the presence of several dependent variables in equations (6) – (9) that make them difficult to be solve, the following similarity functions are introduced

$$\psi=xf(x,y),\quad \theta=\theta(x,y), \tag{10}$$

where ψ is the stream function defined as $u=\frac{\partial\psi}{\partial y}$ and $v=-\frac{\partial\psi}{\partial x}$ which identically satisfied equations (6). The following partial differential equations are generated by substituting equation (10) into equations (6) – (8).

$$\frac{\nu_{hnf}}{\nu_f}\frac{\partial^3 f}{\partial y^3}+\frac{\nu_{hnf}}{\nu_f}We\frac{\partial^2 f}{\partial y^2}\frac{\partial^3 f}{\partial y^3}+f\frac{\partial^2 f}{\partial y^2}-\left(\frac{\partial f}{\partial y}\right)^2 + \frac{(\rho\beta)_{hnf}}{\rho_{hnf}\beta_f}\frac{\sin x}{x}\theta-\frac{\rho_f\sigma_{hnf}}{\rho_{hnf}\sigma_f}M\frac{\partial f}{\partial y}=x\left(\frac{\partial f}{\partial y}\frac{\partial^2 f}{\partial x\partial y}-\frac{\partial f}{\partial x}\frac{\partial^2 f}{\partial y^2}\right), \tag{11}$$

$$\frac{k_{hnf}(\rho C_p)_f}{k_f(\rho C_p)_{hnf}}\frac{1}{\Pr}\frac{\partial^2\theta}{\partial y^2}+f\frac{\partial\theta}{\partial y}+\frac{(\rho C_p)_f}{(\rho C_p)_{hnf}}\lambda\theta=x\left(\frac{\partial f}{\partial y}\frac{\partial\theta}{\partial x}-\frac{\partial f}{\partial x}\frac{\partial\theta}{\partial y}\right). \tag{12}$$

The equations are subjected to transformed boundary conditions

$$f(x,0)=0,\quad \frac{\partial f}{\partial y}(x,0)=0,\quad \theta(x,0)=1,\quad \frac{\partial f}{\partial y}(x,\infty)\to 0,\quad \theta(x,\infty)\to 0, \tag{13}$$

By definition, $M=\frac{\sigma_f a^2 B_o^2}{\rho_f\nu_f Gr^{1/2}}$, $We=\frac{\sqrt{2}x\Gamma\nu_f Gr^{3/4}}{a^2}$, $\Pr=\frac{\nu_f(\rho C_p)_f}{k_f}$, and $\lambda=\frac{a^2 Q_o}{\nu_f Gr^{1/2}(\rho C_p)_f}$ is the magnetic parameter, Williamson parameter, Prandtl number and heat generation parameter, respectively. The details of further hybrid ferrofluid quantities are as follows

$$\frac{\nu_{hnf}}{\nu_f} = \frac{1}{(1-\phi_1)^{2.5}(1-\phi_2)^{2.5}\left[(1-\phi_2)+\left[(1-\phi_1)+\phi_1(\rho_{s1}/\rho_f)\right]+\phi_2(\rho_{s2}/\rho_f)\right]},$$

$$\frac{(\rho\beta)_{hnf}}{\rho_{hnf}\beta_f} = \frac{(1-\phi_2)\left[(1-\phi_1)\rho_f+\phi_1(\rho\beta)_{s1}/\beta_f\right]+\phi_2(\rho\beta)_{s2}/\beta_f}{(1-\phi_2)\left[(1-\phi_1)\rho_f+\phi_1\rho_{s1}\right]+\phi_2\rho_{s2}},$$

$$\frac{k_{hnf}(\rho C_p)_f}{k_f(\rho C_p)_{hnf}} = \frac{k_{hnf}/k_f}{(1-\phi_2)\left[(1-\phi_1)+\phi_1(\rho C_p)_{s1}/(\rho C_p)_f\right]+\phi_2(\rho C_p)_{s2}/(\rho C_p)_f},$$

$$\frac{\rho_{hnf}\left(C_p\right)_f}{\left(\rho C_p\right)_{hnf}} = \frac{(1-\phi_2)\left[(1-\phi_1)\rho_f+\phi_1\rho_{s1}\right]+\phi_2\rho_{s2}}{(1-\phi_2)\left[(1-\phi_1)\rho_f+\phi_1\left(\rho C_p\right)_{s1}/\left(C_p\right)_f\right]+\phi_2\left(\rho C_p\right)_{s2}/\left(C_p\right)_f},$$

$$\frac{\rho_f\sigma_{hnf}}{\rho_{hnf}\sigma_f} = \frac{\sigma_{hnf}/\sigma_f}{(1-\phi_2)\left[(1-\phi_1)+\phi_1\rho_{s1}/\rho_f\right]+\phi_2\rho_{s2}/\rho_f}.$$

The key physical parameters examined in this research are the surface shear stress and the rate of heat transfer. The quantities are represented non-dimensionally by the skin friction coefficient (C_f) and the local Nusselt number (Nu_x), respectively. The mathematical expressions are given as follows

$$C_f = \frac{\tau_w}{\rho_f u_\infty^2}, \qquad Nu_x = \frac{aq_w}{k_f(T_w - T_\infty)}. \tag{14}$$

The surface heat flow q_w and the surface shear stress τ_w are identified as

$$\tau_w = \mu_{hnf}\left(\frac{\partial\bar{u}}{\partial\bar{y}}+\frac{\Gamma}{\sqrt{2}}\left(\frac{\partial\bar{u}}{\partial\bar{y}}\right)^2\right)_{\bar{y}=0}, \qquad q_w = -k_{hnf}\left(\frac{\partial T}{\partial\bar{y}}\right)_{\bar{y}=0}. \tag{15}$$

By using variables in equation (15), the equations of (14) are simplified as

$$C_f Gr^{1/4} = \frac{1}{(1-\phi_1)^{2.5}(1-\phi_2)^{2.5}}\left(x\frac{\partial^2 f}{\partial y^2}+\frac{We}{2}x\left(\frac{\partial^2 f}{\partial y^2}\right)^2\right)_{\bar{y}=0}$$
$$Nu_x Gr^{-1/4} = -\frac{k_{hnf}}{k_f}\left(\frac{\partial\theta}{\partial y}\right)_{\bar{y}=0} \tag{16}$$

Furthermore, the temperature and velocity profiles can be obtained by using the following expressions, respectively.

$$\theta = \theta(x,y), \qquad u = f'(x,y), \tag{17}$$

Figure 2 illustrates the computational flow of the Keller-Box method as applied to the present research for better understanding.

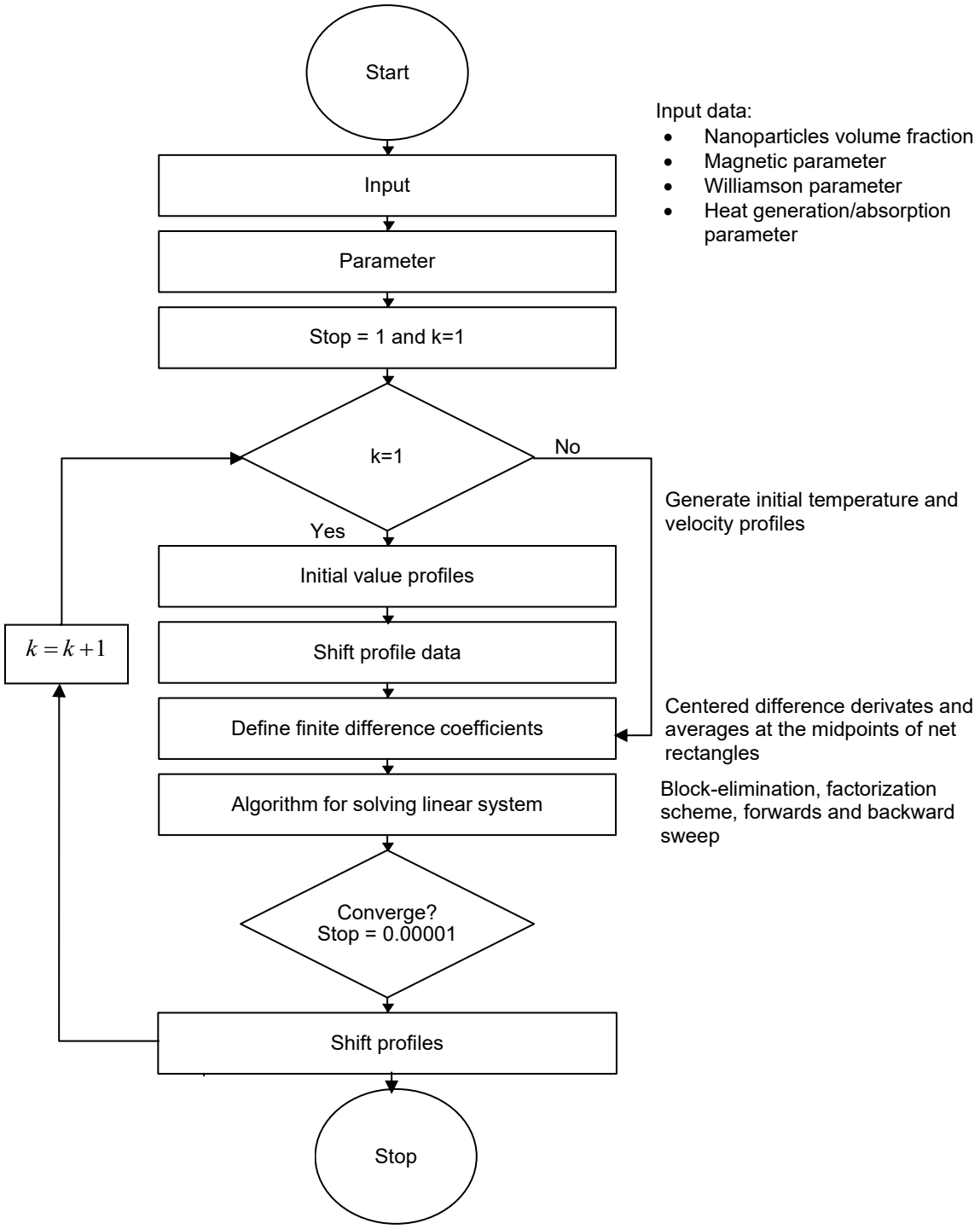

Figure 2. Keller-Box technique flowchart

Results and Discussion

The non-linear governing equations are numerically solved using the implicit finite difference scheme known as the Keller-box method, which has proven to be highly efficient and reliable for boundary layer type problems. This technique incorporates Newton's linearization procedure, transforming the non-linear system into linear algebraic equations and offers unconditional stability, quadratic convergence and robustness. In addition, it is particularly effective for handling nonlinear parabolic differential

equations of any order. The Keller-Box numerical algorithm is implemented in MATLAB to evaluate and illustrate the variations of skin friction coefficient $\left(C_f Gr^{1/4}\right)$, Nusselt number $\left(Nu_x Gr^{-1/4}\right)$, temperature $\left(\theta(y)\right)$, and velocity $\left(f'(y)\right)$ profiles under the influence of various governing parameters such as nanoparticles volume fraction $\left(\phi_1 \text{ and } \phi_2\right)$, magnetic parameter $\left(M\right)$, Williamson parameter $\left(We\right)$, and heat generation/absorption parameter $\left(\lambda\right)$.

In this investigation, the Prandtl number is fixed at 21, reflecting the thermal properties of blood as the base fluid. Four types of fluid model are used in the present study. Following the approach of Devi *et al*. [29], the base fluid is first enhanced by introducing $\phi_1 = 0.1$ of *Fe_3O_4* nanoparticles dispersed into the blood to produce a *Fe_3O_4*-blood ferrofluid. Subsequently, an additional $\phi_2 = 0.06$ volume fraction of gold (*Au*) nanoparticles is incorporated into the *Fe_3O_4*-blood ferrofluid, which resulting in a hybrid ferrofluid designated as *Fe_3O_4-Au*/blood. This fluid is believed to exhibits improved heat transfer capability and thermophysical stability due to the interaction between the metallic and magnetic nanoparticles used. Such hybrid nanofluids are known to provide superior thermal performance compared to conventional single particle ferrofluid, making them suitable for biomedical and thermal management applications. Meanwhile, the ranges of other physical parameters considered in this research are chosen based on previously published works [30-32] to maintain consistency with the literature and to represent realistic conditions relevant to the present physical problem.

To ensure accurate and convergent numerical outcomes, the boundary layer thickness is set to 10, with grid step sizes of $\Delta x = 0.01$ and $\Delta y = 0.02$. The computed solutions are graphically presented to illustrate the effects of various parameters, including the hybrid nanoparticles, magnetic field strength, Williamson fluid characteristics, and heat generation/absorption characteristics.

Table 1 summarizes the thermophysical properties of blood, *Fe_3O_4*, and *Au*. These data were taken from previous literature sources to ensure consistency and reliability in evaluation. To verify the accuracy of present formulation, the numerical findings are compared with those of previously published works. For a fair comparison, the governing equations are reduced to match the limiting cases of earlier models. The comparison, as detailed in Tables 2 and 3, reveals excellent agreement between the current numerical findings and those reported by previous researchers [33,34]

Table 1. Thermophysical characteristics of blood, gold and magnetite ferroparticles

Physical Properties	Blood	Ferrite, *Fe_3O_4* $\left(\phi_1\right)$	Gold, *Au* $\left(\phi_2\right)$
Solid Volume Fraction ρ (kg/m^3)	1063	5180	19300
Specific Heat Capacity of Solid C_p (J/kg.K)	3594	670	129.1
Solid Thermal Conductivity k (W/m.K)	0.492	9.7	318
Solid Thermal Expansion Coefficient	0.000021	0.0000148	0.000013
Electrical Conductivity	0.8	25000	4100000

Figure 3 illustrates the variation of the $C_f Gr^{1/4}$ along the surface of the circular cylinder for different values of ϕ_1 and ϕ_2. It can be observed that the wall shear stress is nearly zero at the stagnation point $\left(x = 0\ rad\right)$, increases rapidly towards the mid-section of the cylinder, and then gradually decreases as the flow approaches the trailing edge. The inclusion of $\phi_1 = 0.1$ in the blood-based fluid leads to an increase in the $C_f Gr^{1/4}$, indicating stronger shear interactions near the wall. When $\phi_2 = 0.06$

nanoparticles are subsequently immersed to form the *Fe₃O₄-Au*/blood hybrid ferrofluid, the $C_f Gr^{1/4}$ attains its maximum value among all tested fluid. This enhancement arises from the higher density and magnetic responsiveness of *Au* nanoparticles compared to Fe_3O_4, which intensify the viscous resistance and shear stress. Consequently, the hybrid ferrofluid demonstrates the highest wall friction, which shows there is a stronger transfer of momentum between the fluid and the cylinder surface.

Table 2. Comparison of $C_f Gr^{1/4}$ with published articles

x	$C_f Gr^{1/4}$		
	Merkin [33]	Molla *et. al.* [34]	Present
0	0.0000	0.0000	0.0000
$\frac{\pi}{6}$	0.4151	0.4145	0.4148
$\frac{\pi}{3}$	0.7558	0.7539	0.7551
$\frac{\pi}{2}$	0.9579	0.9541	0.9562
$\frac{2\pi}{3}$	0.9756	0.9696	0.9665
$\frac{5\pi}{6}$	0.7822	0.7739	0.7725
π	0.3391	0.3264	0.3212

Table 3. Comparison of $Nu_x Gr^{-1/4}$ with published articles

x	$Nu_x Gr^{-1/4}$		
	Merkin [33]	Molla *et. al.* [34]	Present
0	0.4214	0.4241	0.4225
$\frac{\pi}{6}$	0.4161	0.4161	0.4158
$\frac{\pi}{3}$	0.4007	0.4005	0.4012
$\frac{\pi}{2}$	0.3745	0.3740	0.3741
$\frac{2\pi}{3}$	0.3364	0.3355	0.3374
$\frac{5\pi}{6}$	0.2825	0.2812	0.2831
π	0.1945	0.1917	0.2124

Figure 4 presents the distribution of $Nu_x Gr^{-1/4}$ along the cylinder surface for various ϕ_1 and ϕ_2. The maximum heat transfer rate is observed near the stagnation region, where the temperature gradient at the wall is strongest. As the flow progresses downstream, the $Nu_x Gr^{-1/4}$ gradually decreases reflecting a reduction in convective dominance and an increase in conductive heat transfer effects. The addition of

$\phi_1 = 0.1$ enhances the thermal conductivity of the base fluid, thereby increasing the $Nu_x Gr^{-1/4}$ relative to pure blood. When $\phi_2 = 0.06$ are further incorporated, the *Fe₃O₄-Au*/blood hybrid ferrofluid exhibits the highest $Nu_x Gr^{-1/4}$, confirming the superior thermal transport capability of hybrid nanoparticle suspensions. This improvement is attributed to *Au*'s excellent thermal conductivity and strong Brownian motion contribution, which augment the overall energy transport in the fluid. The results clearly demonstrate that by combining *Fe₃O₄* and *Au* nanoparticles, leads to improved convective heat transfer performance compared to single component ferrofluids.

The influence of ϕ_1 and ϕ_2 on the $\theta(y)$ distribution is depicted in Figure 5. It is shown that the $\theta(y)$ decreases steadily as the distance from the cylinder surface increases, which is expected since heat moves from the hot wall to the cooler surrounding fluid. An increase in nanoparticle concentration slightly elevates the temperature near the wall region and broadens the thermal boundary layer. This trend arises because suspended nanoparticles enhance the effective thermal conductivity of the fluid, promoting greater energy diffusion through the medium. Consequently, the immersion of ϕ_1 and ϕ_2 nanoparticles results in a mild thickening of the thermal layer compared to the base fluid, with the hybrid ferrofluid exhibiting the most significant temperature gradient near the surface. The improved thermal response of the *Fe₃O₄-Au*/blood hybrid ferrofluid suggests a more efficient energy transport mechanism, consistent with the elevated $Nu_x Gr^{-1/4}$ reported in Figure 4.

Figure 6 displays the $f'(y)$ of the fluid for ϕ_1 and ϕ_2. The $f'(y)$ initially rises from zero at the wall due to the no-slip condition, reaches a peak within the boundary layer, and subsequently decays to zero as it approaches the free stream. The addition of ϕ_1 and ϕ_2 increases the fluid's momentum diffusion, resulting in a noticeable enhancement in near wall velocity magnitude. Among all tested fluids, The *Fe₃O₄-Au*/blood hybrid ferrofluid shows the highest peak $f'(y)$, confirming its superior flow momentum characteristics. However, it's $f'(y)$ also decays more sharply beyond the peak, indicating a thinner hydrodynamic boundary layer compared to the *Fe₃O₄*-blood ferrofluid. This behaviour reflects the interplay between increased density an viscous resistance in the hybrid fluid, which amplifies frictional effects at the wall, as observed in Figure 3. Physically, this implies that although hybrid ferrofluids can accelerate flow near the surface, they also experience stronger damping effects due to intensified wall interactions.

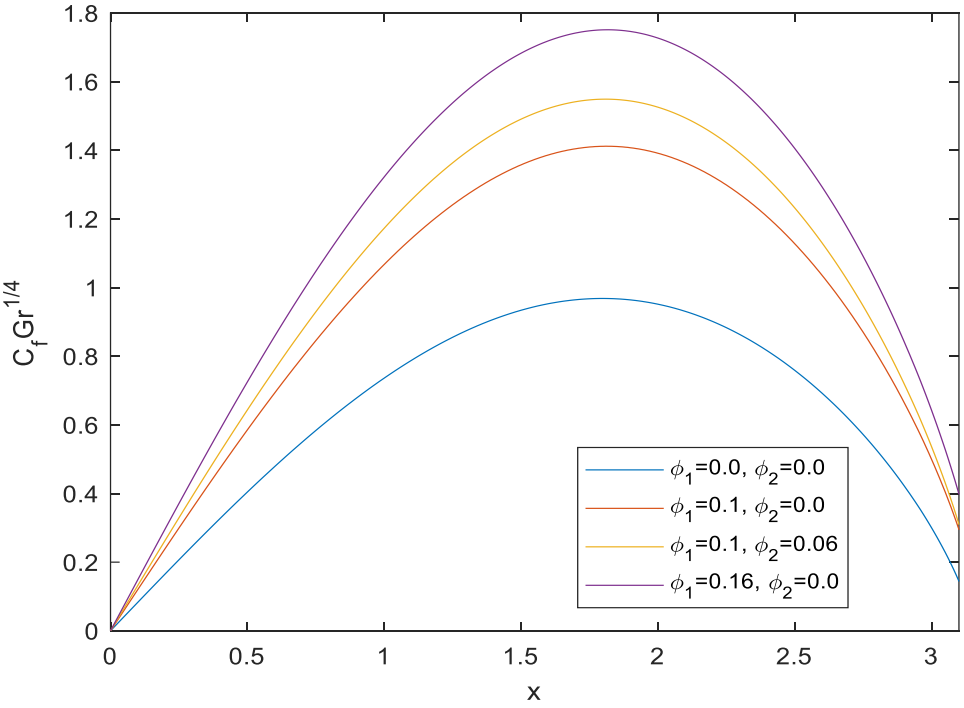

Figure 3. Skin Friction coefficient, $C_f Gr^{1/4}$ variation versus *x* for different ϕ_1 and ϕ_2

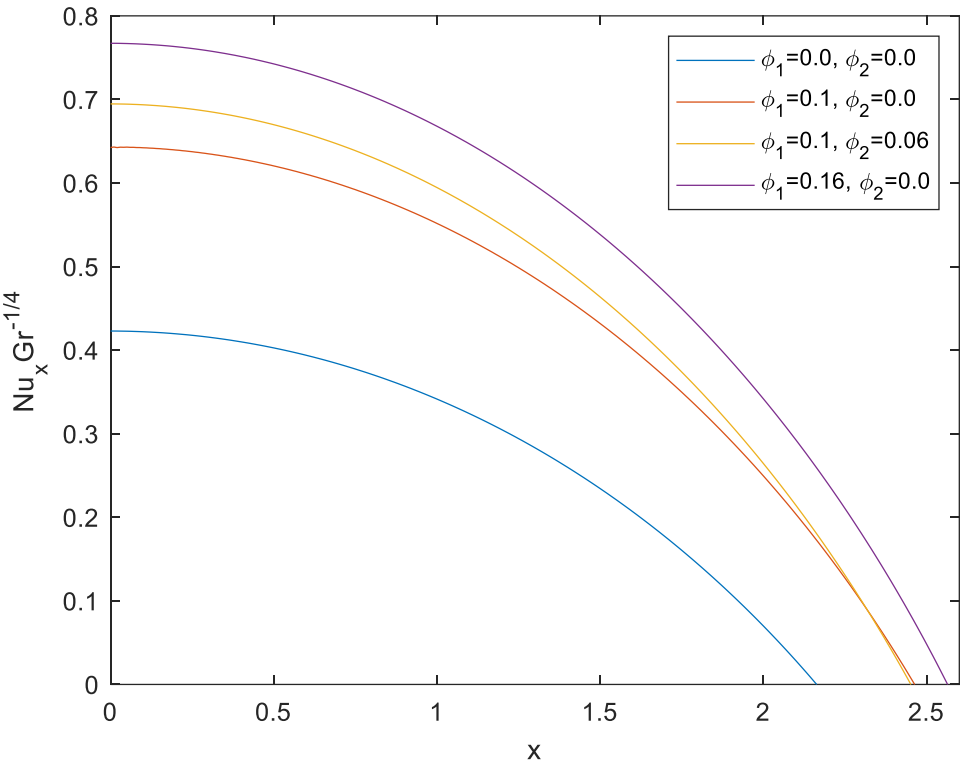

Figure 4. Nusselt number, $Nu_x Gr^{-1/4}$ variation versus *x* for different ϕ_1 and ϕ_2

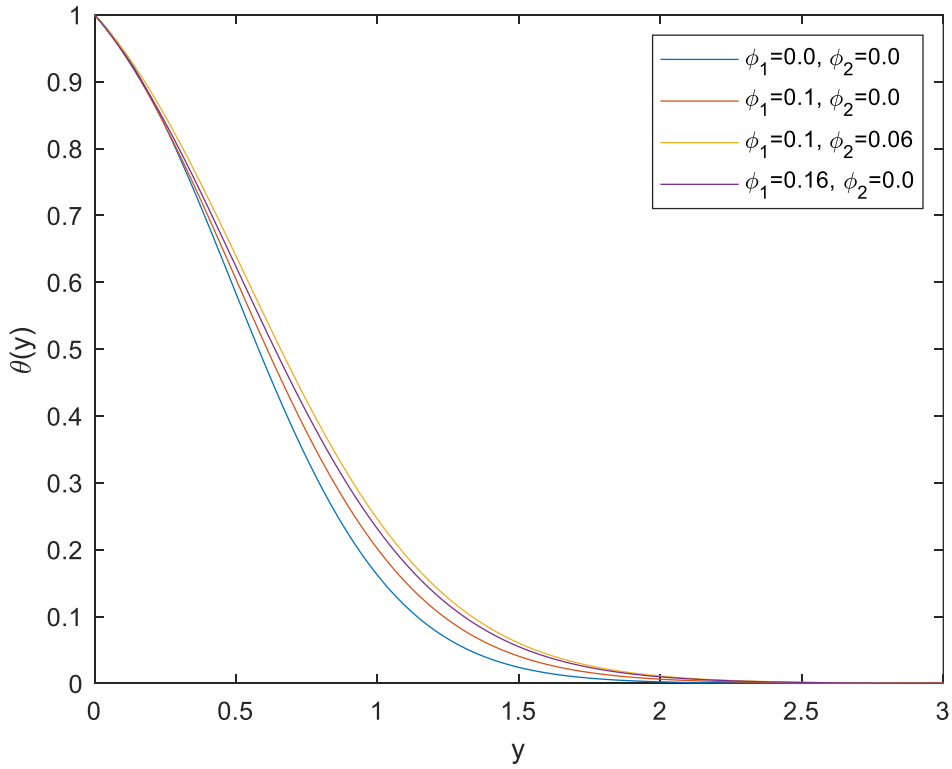

Figure 5. Temperature Profile, $\theta(y)$ variation versus *y* for different ϕ_1 and ϕ_2

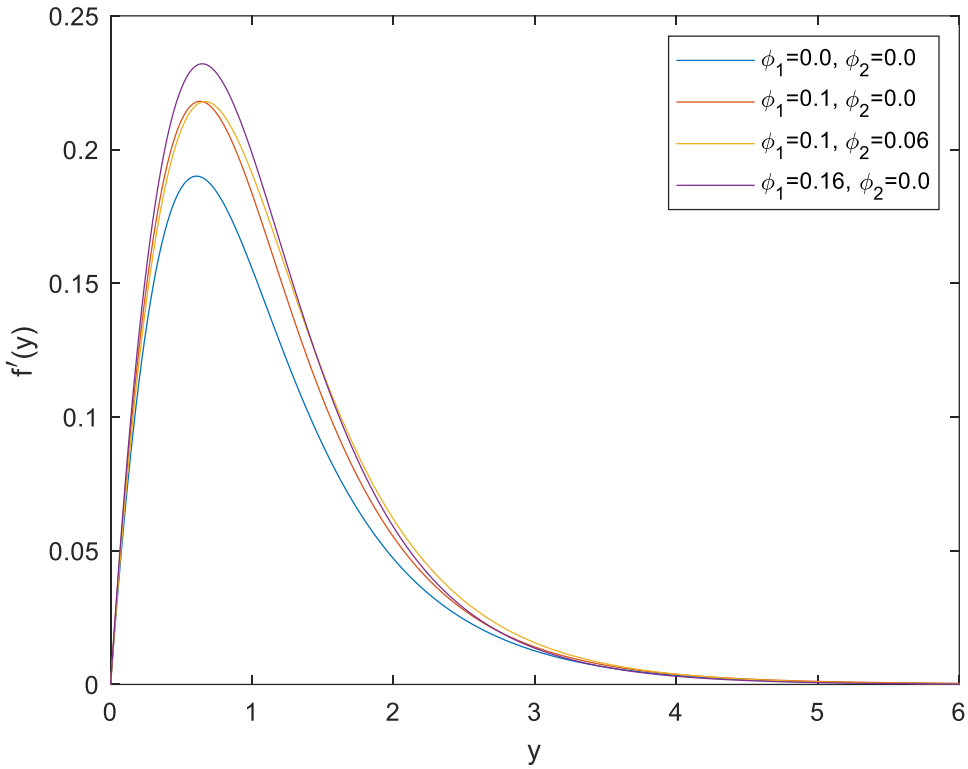

Figure 6. Velocity profiles, $f'(y)$ variation versus *y* for different ϕ_1 and ϕ_2

Figure 7 illustrates the variation $C_f Gr^{1/4}$ of for different values of *M*. An increase in *M* results in a consistent reduction in $C_f Gr^{1/4}$. This trend occurs because a stronger magnetic field enhances the Lorentz force, which opposes fluid motion and introduces an electromagnetic drag. The resulting deceleration lowers the near-wall velocity gradient and subsequently diminishes the wall shear stress. Thus, stronger *M* slows down the flow near the wall, which reduces the friction between the fluid and the cylinder surface. Meanwhile, the influence of *M* on the $Nu_x Gr^{-1/4}$ is presented in Figure 8. The figure shows that $Nu_x Gr^{-1/4}$ decreases as *M* increases, indicating a decline in convective heat transfer. The magnetic field dampens the fluid motion, thereby weakening the thermal energy transport from the wall to the fluid. This suppression reduces the temperature gradient at the surface, resulting in lower heat transfer rates. Therefore, stronger magnetic fields help control and steady the flow but make heat transfer less effective.

Next, Figure 9 depicts the $\theta(y)$ profile for different *M* values. It is clear that higher *M* values lead to elevated $\theta(y)$ distribution and a thicker thermal boundary layer. The increased Lorentz force he increased Lorentz force restricts the fluid motion and promotes heat accumulation near the wall. Furthermore, the electromagnetic drag induces additional resistive heating, which enhances the local temperature of the fluid. Consequently, the rate of temperature decay away from the wall becomes slower under stronger magnetic effects. In Figure 10, the $f'(y)$ corresponding to various *M* is discussed. As *M* increases, the velocity magnitude and the boundary layer thickness decrease notably. This reduction arises from the retarding influence of the Lorentz force, which acts in the opposite direction to the fluid motion. The suppressed velocity field directly corresponds to the decline in the skin friction coefficient discussed in Figure 7. Overall, when *M* increases, the flow becomes more stable and easier to control magnetically, but the fluid loses some momentum and heat transfer ability.

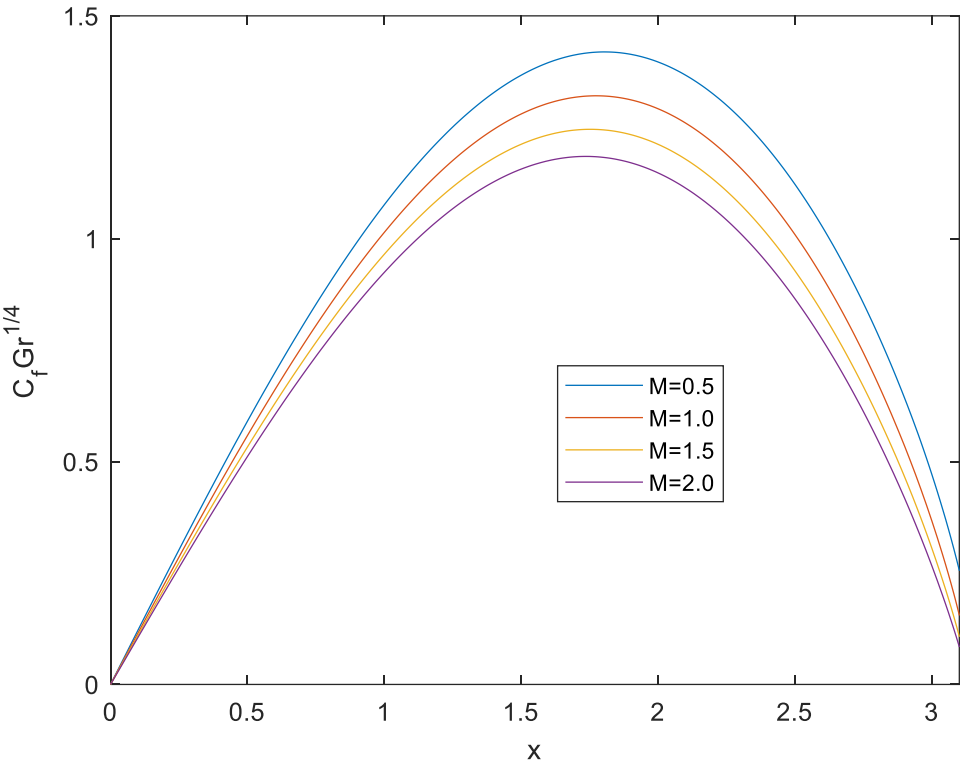

Figure 7. Skin Friction coefficient, $C_f Gr^{1/4}$ variation versus *x* for different M

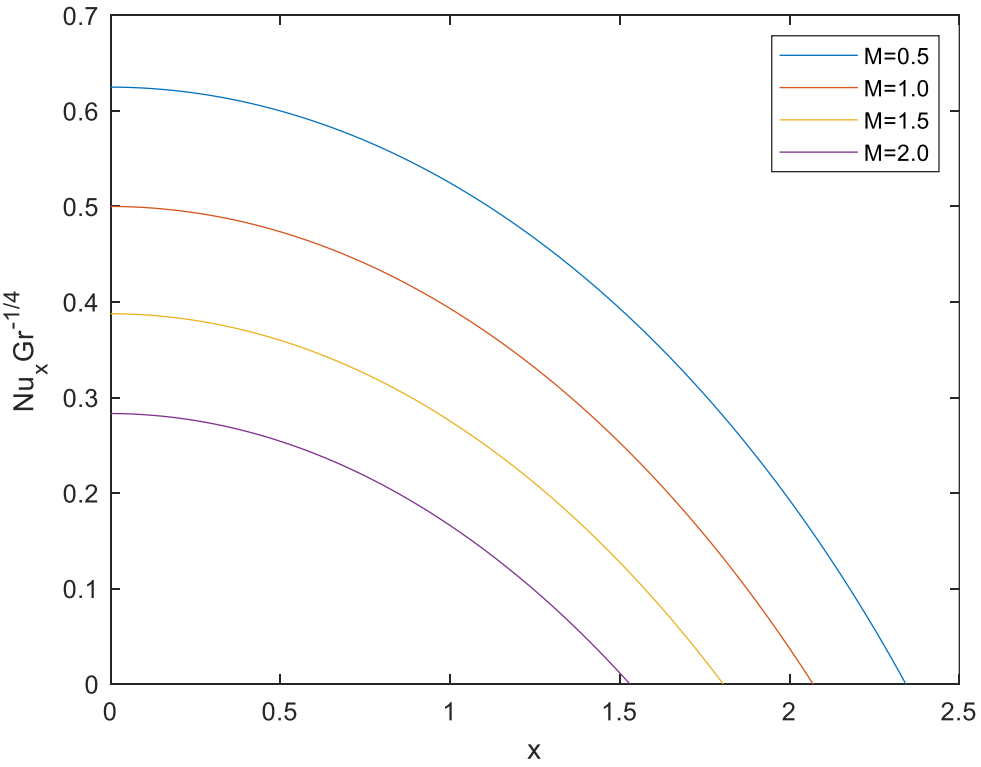

Figure 8. Nusselt number, $Nu_x Gr^{-1/4}$ variation versus *x* for different M

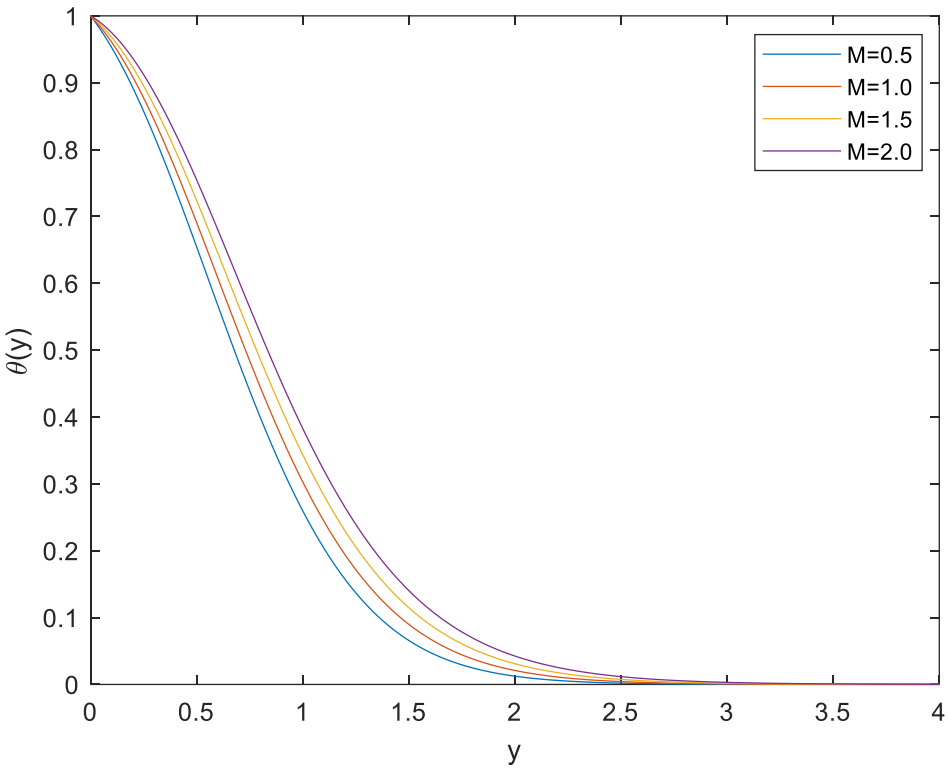

Figure 9. Temperature Profile, $\theta(y)$ variation versus *y* for different M

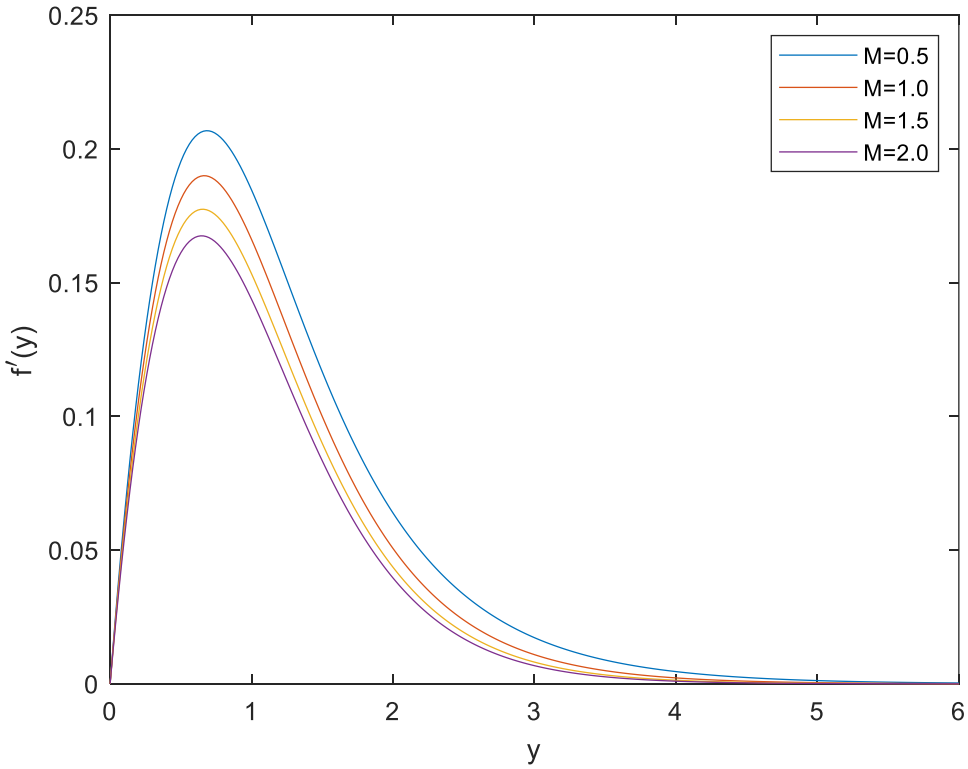

Figure 10. Velocity profiles, $f'(y)$ variation versus *y* for different M

The effects of different values of *We* are shown in Figures 11-14. Figure 11 illustrates the variation of $C_f Gr^{1/4}$. It can be observed that $C_f Gr^{1/4}$ increases slightly with *We.* This occurs because a higher *We* corresponds to a weaker shear-thinning effect, which enhances the effective viscosity of the hybrid ferrofluid. As a result, the resistance between the fluid and the cylinder surface increases, leading to higher wall shear stress. Physically, this means that the fluid becomes less pseudoplastic as *We* rises, thereby intensifying the frictional effects at the surface. Meanwhile, Figure 12 presents the variation of $Nu_x Gr^{-1/4}$ for various *We.* The results show a gradual decrease in $Nu_x Gr^{-1/4}$ as *We* increases, indicating a decline in convective heat transfer. This can be attributed to the rise in viscosity at higher *We,* which weakens the convective currents and reduces the temperature gradient near the wall. Consequently, the hybrid ferrofluid exhibits lower thermal transport efficiency as the Williamson parameter grows, reflecting the suppression of convective mechanisms due to enhanced fluid resistance.

Figure 13 and 14 depicts the $\theta(y)$ and $f'(y)$, for different *We* values, respectively. The curves on Figure 13 show that $\theta(y)$ decreases more slowly as *We* increases, implying a thicker thermal boundary layer. This occurs because higher *We* values slow down the fluid motion, allowing more heat to accumulate near the surface. Hence, the increased viscous resistance enhances the fluid's capacity to retain heat within the boundary layer, slightly raising the overall $\theta(y)$. Figure 14 shows an increasing *We* results in a slight reduction in the peak velocity and a thinning of the velocity boundary layer. This behavior is consistent with the nature of the Williamson fluid model, where higher *We* reduces the shear-thinning effect, leading to slower flow development. Physically, this means that as *We* increases, the fluid's ability to stretch and accelerate decreases, resulting in a smaller velocity gradient near the wall and a weaker overall momentum transfer.

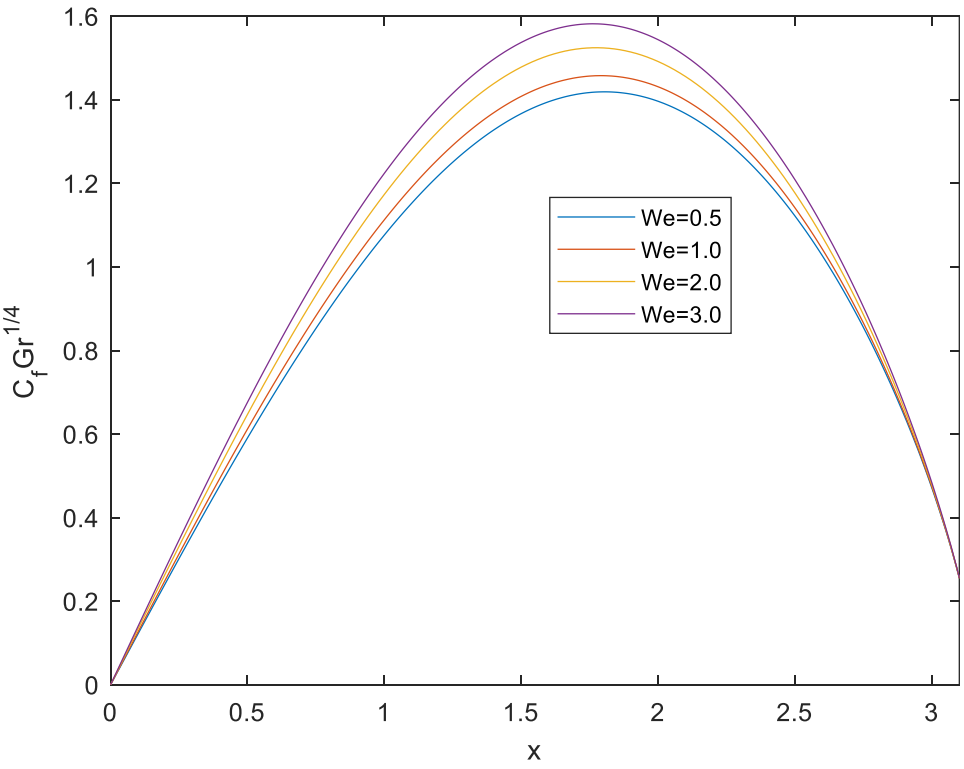

Figure 11. Skin Friction coefficient, $C_f Gr^{1/4}$ variation versus *x* for different We

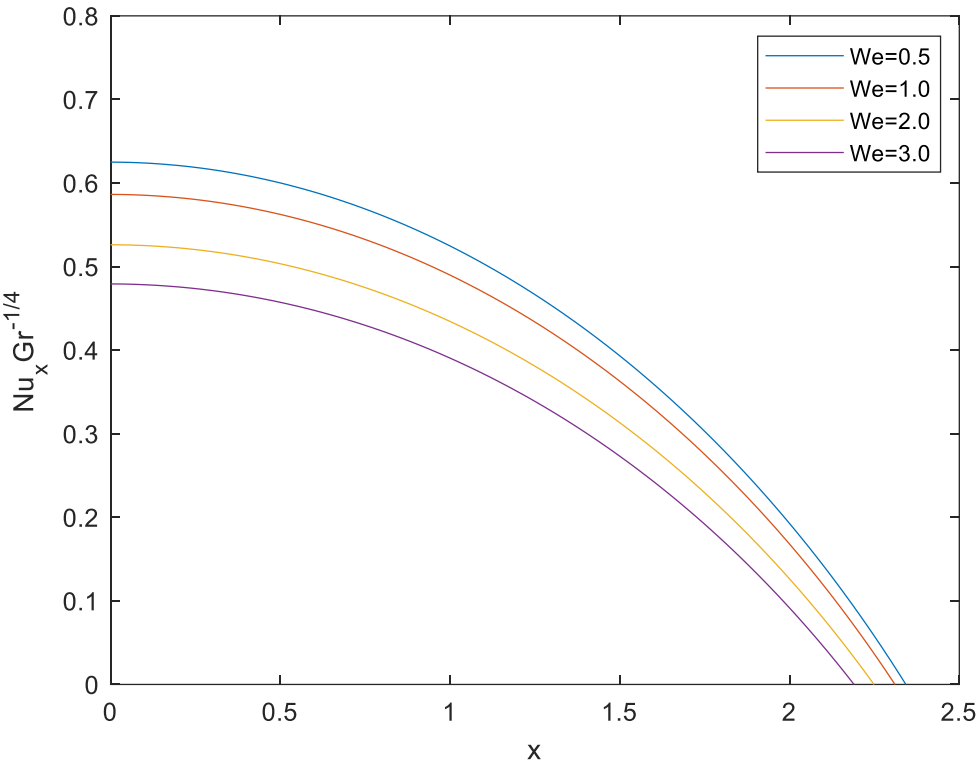

Figure 12. Nusselt number, $Nu_x Gr^{-1/4}$ variation versus *x* for different We

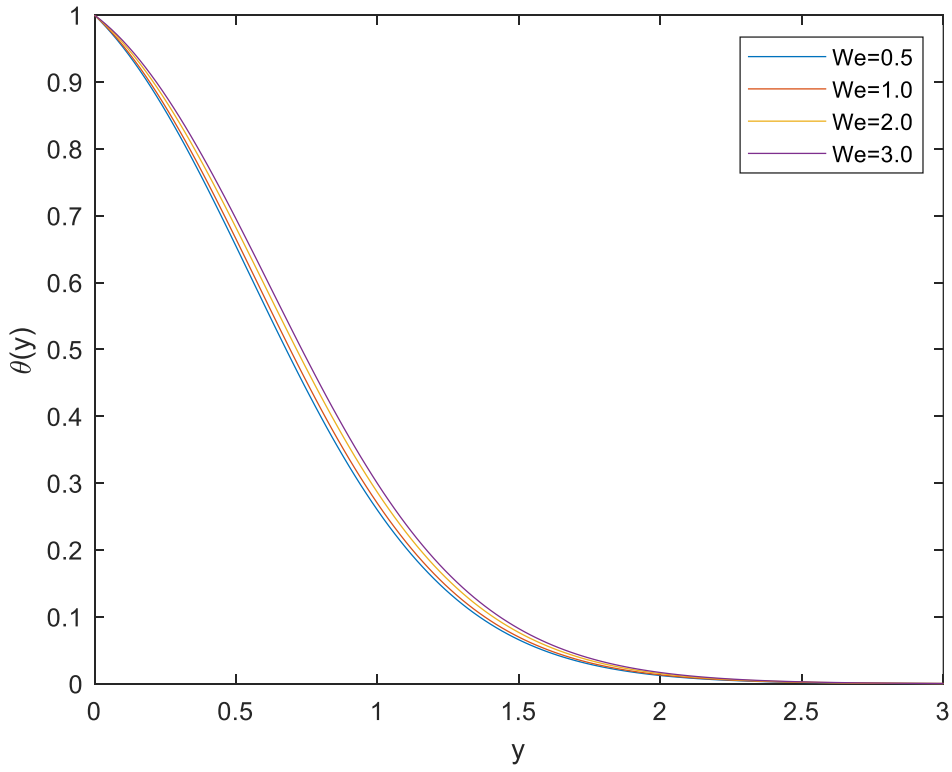

Figure 13. Temperature Profile, $\theta(y)$ variation versus *y* for different We

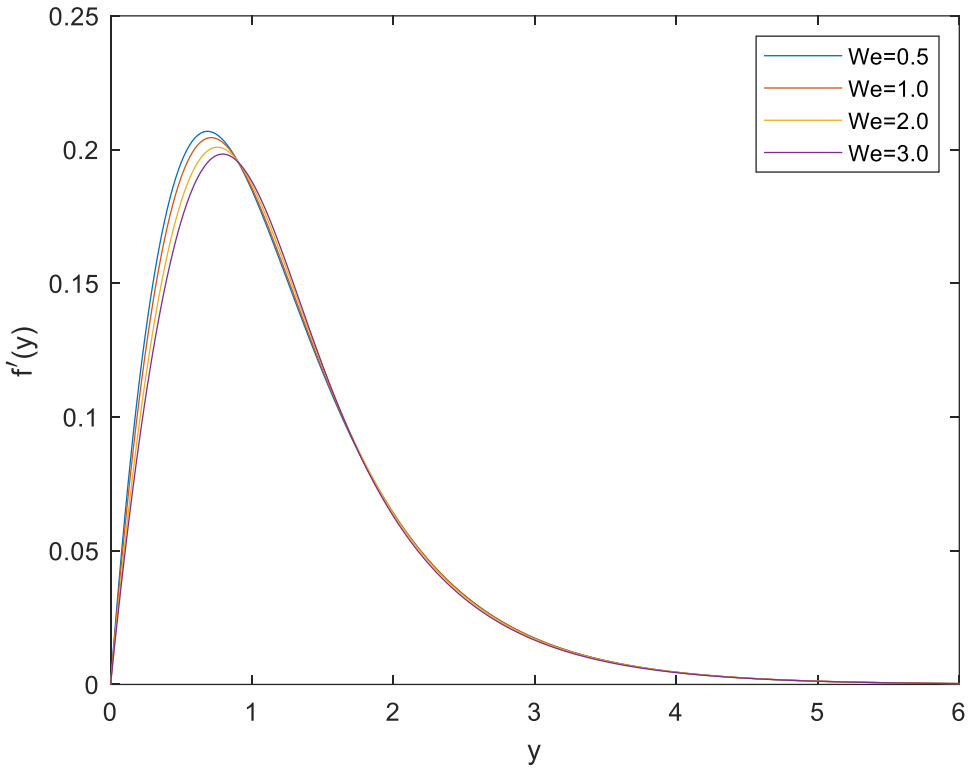

Figure 14. Velocity profiles, $f'(y)$ variation versus *y* for different We

Figure 15 shows the variation of $C_f Gr^{1/4}$ for different values of λ. Here, λ represent how much heat is being generated or absorbed inside the fluid. It is observed that as λ increases, the $C_f Gr^{1/4}$ also increases at every point along the surface, with a noticeable peak occurring near the mid-region of the cylinder. The values of $\lambda = -0.2$ produced the lowest friction $C_f Gr^{1/4}$, while $\lambda = 0.1$ has the highest. This trend occurs because the internal heat generation raises the fluid temperature, which increases buoyancy force and drives stronger fluid motion near the surface. The resulting increase in velocity gradients at the wall leads to higher shear stress and $C_f Gr^{1/4}$. In contrast, internal heat absorption reduces the thermal driving force, weakens the velocity boundary layer, and lowers wall shear. Therefore, the λ plays a key role in controlling momentum transfer near the surface.

In Figure 16, the values of $Nu_x Gr^{-1/4}$ is plotted for various λ values. Here, a clear decreasing trend of $Nu_x Gr^{-1/4}$ is seen as λ increase. The highest heat transfer rate occurs for $\lambda = -0.2$, indicating the internal heat absorption enhances the temperature gradient near the surface, allowing more heat to leave the cylinder. This steep temperature gradient enhances the rate of heat transfer from the surface, resulting in a higher $Nu_x Gr^{-1/4}$. In contrast, when $\lambda = 0.1$, internal heat is being supplied to the fluid, which raises the bulk fluid temperature and reduces the temperature difference near the wall. This weaker gradient leads to lower surface heat transfer and a smaller $Nu_x Gr^{-1/4}$. In addition, the drop in $Nu_x Gr^{-1/4}$ indicates that heat is transferred mainly by conduction rather than convection near the cylinder surface. According to Elbashbesy *et al*. [35], essentially, $\lambda < 0$ draws energy from the system and encourages more heat flow from the surface, while $\lambda > 0$ reduces the need for external heating, thereby lowering the heat flux.

Figure 17 illustrates $\theta(y)$ varies under different λ. Increasing λ results in a thicker thermal boundary layer and higher fluid temperature farther from the wall. For $\lambda = 0.1$, the temperature drops more slowly, meaning heat is distributed deeper into the fluid. While $\lambda = -0.2$, the fluid absorbs heat internally, the temperature decreases rapidly, indicating a cooler and thinner thermal region. This is because absorbed heat removes energy from the fluid, reducing the temperature throughout the boundary layer. Thus, $\lambda < 0$ accelerates cooling and sharpens the temperature gradient near the wall, while $\lambda > 0$ maintains higher temperatures in the fluid. In Figure 18, as λ increases, the $f'(y)$ near surface becomes higher, and boundary layer grows thicker. This is because $\lambda > 0$ raises the fluid temperature, which strengthen the buoyancy forces and enhances the upward flow. In contrast, $\lambda < 0$ cools the fluid and weakens the buoyancy effect, resulting in lower $f'(y)$ and a thinner boundary layer. These results show that $\lambda > 0$ promotes stronger natural convection, while $\lambda < 0$ suppresses it.

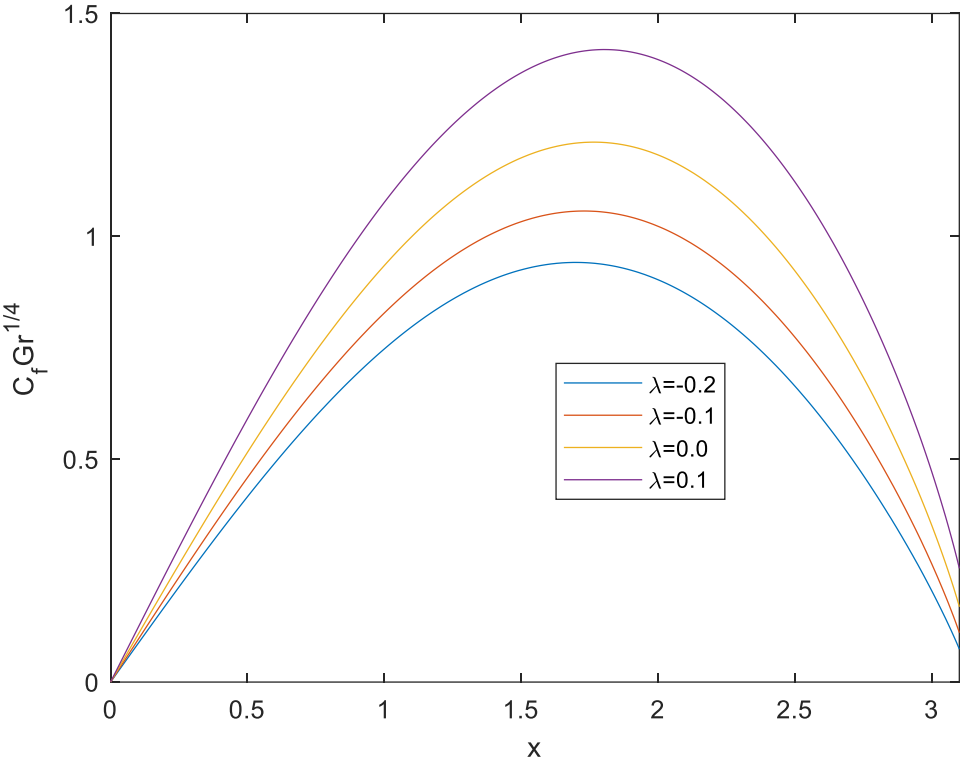

Figure 15. Skin Friction coefficient, $C_f Gr^{1/4}$ variation versus *x* for different λ.

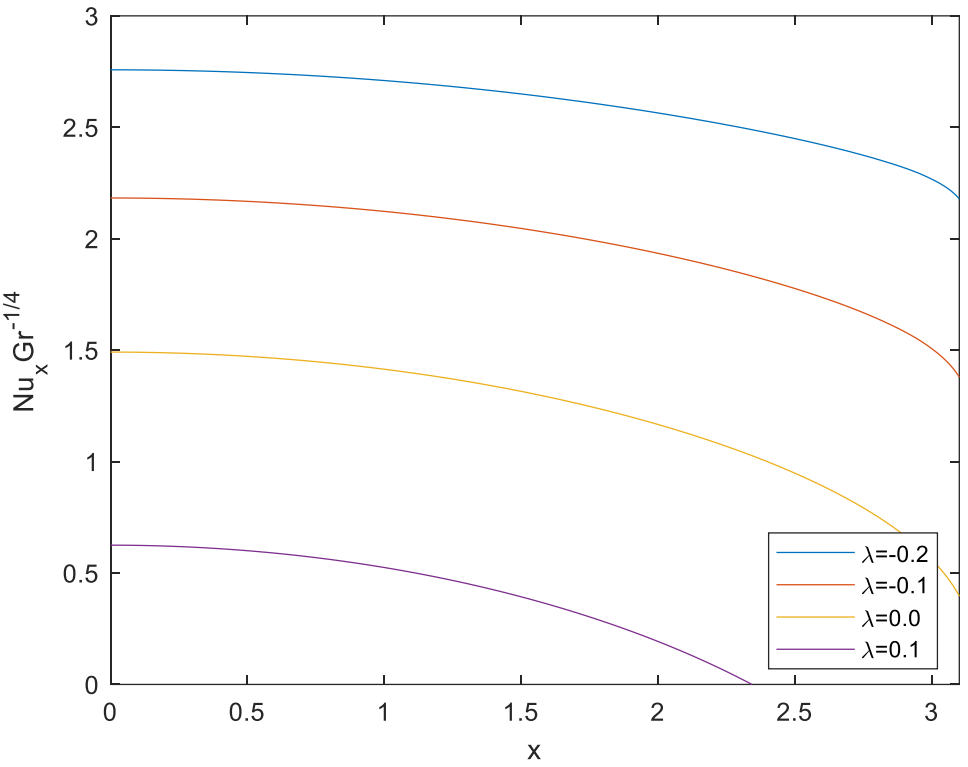

Figure 16. Nusselt number, $Nu_x Gr^{-1/4}$ variation versus *x* for different λ.

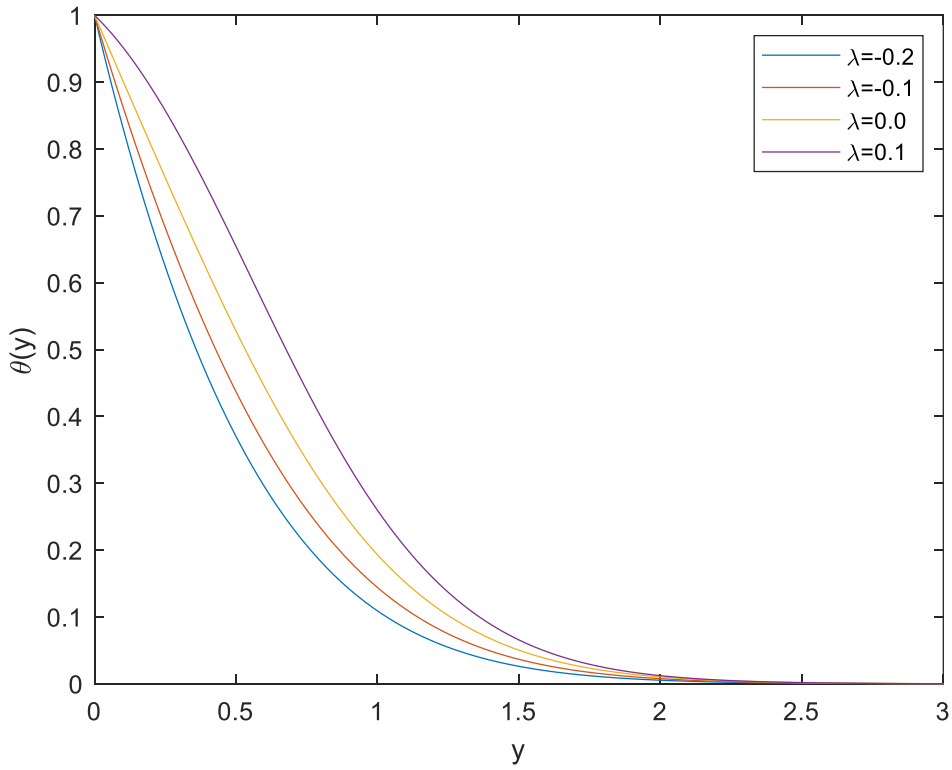

Figure 17. Temperature Profile, $\theta(y)$ variation versus *y* for different λ.

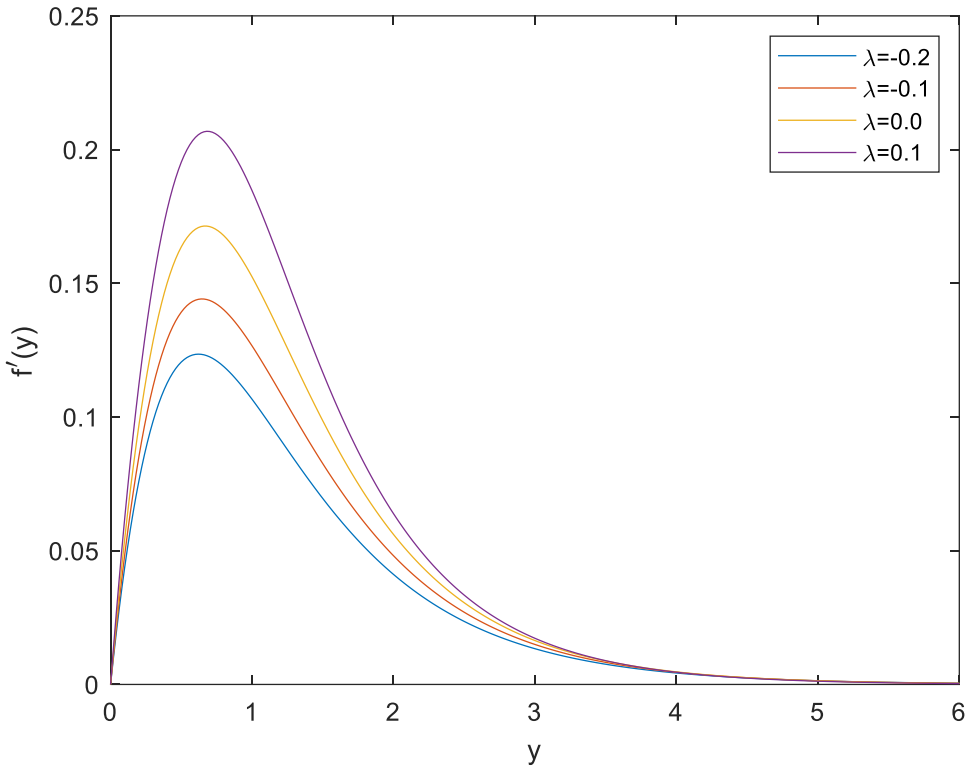

Figure 18. Velocity profiles, $f'(y)$ variation versus *y* for different λ.

Conclusions

This research presents a numerical study using Keller-box method of the free convection boundary layer flow over a horizontal circular cylinder in a hybrid Williamson ferrofluid. The consequences of the volume percentage of ferrite nanoparticles and gold nanoparticles, the magnetic parameter, the Williamson parameter and the heat generation/absoprtion in the hybrid Williamson ferrofluid affecting the skin friction coefficient, the Nusselt number, the temperature profile, and the velocity profile are demonstrated. The present findings have practical significance in both engineering and biomedical applications. The improved heat transfer and magnetic control of the based Williamson hybrid ferrofluid can enhance the efficiency of cooling systems, heat exchangers, and magnetic medical treatments. These insight contribute to the development of more effective and energy-efficient thermal management technologies. The following is a summary of the study that may be drawn from it:

i. The $C_f Gr^{1/4}$ and the $Nu_x Gr^{-1/4}$ increase with the addition of ϕ_1 and ϕ_2, indicating improved thermal conductivity and stronger wall shear interaction.

ii. At equal ϕ_1 and ϕ_2, the Williamson hybrid ferrofluid exhibits higher convective heat transfer performance and greater frictional effects than single component ferrofluids.

iii. An increase in the *We* enhances the non-Newtonian fluid's characteristics, causing greater resistance to flow, reduced velocity and heat transfer rates, and a slight thickening of the boundary layers.

iv. As the *M* increases, the stronger Lorentz force slows the fluid motion, reducing $f'(y)$, $C_f Gr^{1/4}$ and $Nu_x Gr^{-1/4}$, while thinning the velocity boundary layer and thickening the thermal layer.

v. Increasing the λ elevates the boundary layer temperature, thickens the thermal boundary layer, and reduces the $Nu_x Gr^{-1/4}$ by weakening the temperature gradient at the surface.

Conflicts of Interest

The authors declare that there is no conflict of interest regarding the publication of this paper.

Acknowledgment

The author would like to thank the Ministry of Higher Education Malaysia for providing financial support under Fundamental Research Grant Scheme (FRGS) No. FRGS/1/2023/STG06/UMP/02/1 (University reference: RDU230111) and Universiti Malaysia Pahang Al-Sultan Abdullah under Post-Graduate Research Scheme (PGRS2303143).

References

[1] Kumar, A., Dutt, N., & Awasthi, M. K. (Eds.). (2024). *Heat transfer enhancement techniques: Thermal performance, optimization and applications.* John Wiley & Sons.
[2] Mauri, R. (2023). Free convection. In *Transport phenomena in multiphase flows* (pp. 315–331). Springer International Publishing.
[3] Yu, W., France, D. M., Routbort, J. L., & Choi, S. U. (2008). Review and comparison of nanofluid thermal conductivity and heat transfer enhancements. *Heat Transfer Engineering, 29*(5), 432–460.
[4] Choi, S. U. (1995). Enhancing thermal conductivity of fluids with nanoparticles. In *ASME International Mechanical Engineering Congress and Exposition* (Vol. 17421, pp. 99–105). American Society of Mechanical Engineers.
[5] Eastman, J. A., Choi, S. U. S., Li, S., Yu, W., & Thompson, L. J. (2001). Anomalously increased effective thermal conductivities of ethylene glycol-based nanofluids containing copper nanoparticles. *Applied Physics Letters, 78*(6), 718–720.
[6] Keblinski, P., Phillpot, S. R., Choi, S. U. S., & Eastman, J. A. (2002). Mechanisms of heat flow in suspensions of nano-sized particles (nanofluids). *International Journal of Heat and Mass Transfer, 45*(4), 855–86
[7] Borode, A., Tshephe, T., & Olubambi, P. (2025). A critical review of the thermophysical properties and applications of carbon-based hybrid nanofluids in solar thermal systems. *Frontiers in Energy Research, 12,* 1509437.
[8] Mohamed, M. K. A., Noar, N. A. Z. M., Salleh, M. Z., & Ishak, A. (2019). Free convection boundary layer flow on a solid sphere in a nanofluid with viscous dissipation. *Malaysian Journal of Fundamental and Applied Sciences, 15*(3), 381–388.
[9] Koo, K. N., Ismail, A. F., Othman, M. H. D., Bidin, N., & Rahman, M. A. (2019). Preparation and characterization of superparamagnetic magnetite (Fe_3O_4) nanoparticles: A short review. *Malaysian Journal of Fundamental and Applied Sciences, 15*(1), 23–31.
[10] Papell, S. S. (1965). *Low viscosity magnetic fluid obtained by the colloidal suspension of magnetic particles* (U.S. Patent No. 3,215,572). United States Patent Office.
[11] Oehlsen, O., Cervantes-Ramírez, S. I., Cervantes-Avilés, P., & Medina-Velo, I. A. (2022). Approaches on ferrofluid synthesis and applications: Current status and future perspectives. *ACS Omega, 7*(4), 3134–3150.
[12] Yang, W., Zhang, Y., Yang, X., Sun, C., & Chen, Y. (2022). Systematic analysis of ferrofluid: A visualization review, advances, engineering applications, and challenges. *Journal of Nanoparticle Research, 24*(6), 102.
[13] Huang, X., Saadat, M., Bijarchi, M. A., & Shafii, M. B. (2023). Ferrofluid double emulsion generation and manipulation under magnetic fields. *Chemical Engineering Science, 270,* 118519.
[14] Wang, Y., Li, Z., Li, D., Chen, F., Zhao, Q., Qing, J., ... & Zhao, Y. (2024, August). A double-rotating ferrofluid vane micropump with an embedded fixed magnet. *Actuators, 13*(8).
[15] Ilias, M. R., Rawi, N. A., & Shafie, S. (2017). Natural convection of ferrofluid from a fixed vertical plate with aligned magnetic field and convective boundary condition. *Malaysian Journal of Fundamental and Applied Sciences, 13*(3).
[16] Abdelsalam, S. I., & Bhatti, M. M. (2019). New insight into AuNP applications in tumour treatment and cosmetics through wavy annuli at the nanoscale. *Scientific Reports, 9*(1).
[17] Abdullah, N., & Ismail, Z. (2022). Finite element analysis of biomagnetic fluid flow in a channel with an overlapping stenosis. *Malaysian Journal of Fundamental and Applied Sciences, 18*(6), 618–629.
[18] Idris, S., Jamaludin, A., Nazar, R., & Pop, I. (2023). Heat transfer characteristics of magnetized hybrid ferrofluid flow over a permeable moving surface with viscous dissipation effect. *Heliyon, 9*(5).
[19] Swalmeh, M. Z., Alwawi, F. A., Kausar, M. S., Ibrahim, M. A. H., Hamarsheh, A. S., Sulaiman, I. M., ... & Panyanak, B. (2023). Numerical simulation on energy transfer enhancement of a Williamson ferrofluid subjected to thermal radiation and a magnetic field using hybrid ultrafine particles. *Scientific Reports, 13*(1), 3176.
[20] Rauf, A., Mushtaq, A., Shah, N. A., & Botmart, T. (2022). Heat transfer and hybrid ferrofluid flow over a nonlinearly stretchable rotating disk under the influence of an alternating magnetic field. *Scientific Reports, 12*(1), 17548.
[21] Williamson, R. V. (1929). The flow of pseudoplastic materials. *Industrial & Engineering Chemistry, 21*(11), 1108–1111.
[22] Stueber, D. D., Villanova, J., Aponte, I., Xiao, Z., & Colvin, V. L. (2021). Magnetic nanoparticles in biology and medicine: Past, present, and future trends. *Pharmaceutics, 13*(7), 943.
[23] Liu, J. F., Jang, B., Issadore, D., & Tsourkas, A. (2019). Use of magnetic fields and nanoparticles to trigger

drug release and improve tumor targeting. *Wiley Interdisciplinary Reviews: Nanomedicine and Nanobiotechnology, 11*(6), e1571.

[24] Zhang, Y. F., & Lu, M. (2024). Advances in magnetic induction hyperthermia. *Frontiers in Bioengineering and Biotechnology, 12,* 1432189.

[25] Mahat, R., Rawi, N. A., Kasim, A. R. M., & Shafie, S. (2020). Heat generation effect on mixed convection flow of viscoelastic nanofluid: Convective boundary condition solution. *Malaysian Journal of Fundamental and Applied Sciences, 16*(2), 166–172.

[26] Bing, K. Y., Abid, H., Muhammad, K., & Zuki, S. M. (2019). Heat and mass transfer analysis on flow of Williamson nanofluid with thermal and velocity slips: Buongiorno model. *Propulsion and Power Research, 8*(3), 243–252.

[27] Mohamed, M. K. A., Salleh, M. Z., Jamil, F. C., & Ruey, O. H. (2021). Free convection boundary layer flow over a horizontal circular cylinder in Al_2O_3–Ag/water hybrid nanofluid with viscous dissipation. *Malaysian Journal of Fundamental and Applied Sciences, 17*(1), 20–25.

[28] Swalmeh, M. Z., Alkasasbeh, H. T., Hussanan, A., & Mamat, M. (2018). Heat transfer flow of Cu–water and Al_2O_3–water micropolar nanofluids about a solid sphere in the presence of natural convection using Keller-Box method. *Results in Physics, 9,* 717–724.

[29] Devi, S. U., & Devi, D. (2017). Heat transfer enhancement of Cu–Al_2O_3/water hybrid nanofluid flow over a stretching sheet. *Journal of the Nigerian Mathematical Society, 36,* 419–433.

[30] Razzaq, I., Xinhua, W., Rasool, G., Sun, T., Thumma, T., Reddy, C. A., ... & Khan, A. Q. (2024). Effects of viscous and Joule dissipation on hydromagnetic hybrid nanofluid flow over nonlinear stretching surface with Hamilton–Crosser model. *Case Studies in Thermal Engineering, 61,* 105125.

[31] Govindaraj, N., & Singh, A. K. (2024). Numerical computation of Williamson hybrid nanofluid flow over curved surfaces with effects of thermal radiation. *ASME Journal of Heat and Mass Transfer, 146*(1).

[32] Gambo, J. J., & Gambo, D. (2021). On the effect of heat generation/absorption on magnetohydrodynamic free convective flow in a vertical annulus: An Adomian decomposition method. *Heat Transfer, 50*(3), 2288–2302.

[33] Merkin, J. H. (1976). Free convection boundary layer on an isothermal horizontal cylinder. *American Society of Mechanical Engineers and American Institute of Chemical Engineers.*

[34] Molla, M. M., Hossain, M. A., & Paul, M. C. (2006). Natural convection flow from an isothermal horizontal circular cylinder in presence of heat generation. *International Journal of Engineering Science, 44*(13–14), 949–958.

[35] Elbashbeshy, E. M., Asker, H. G., & Nagy, B. (2022). The effects of heat generation and absorption on boundary layer flow of a nanofluid containing gyrotactic microorganisms over an inclined stretching cylinder. *Ain Shams Engineering Journal, 13*(5), 101690.